CHEMISTRY OF MATERIALS

pubs.acs.org/cm

Methods/Protocols

Transient Thermoreflectance with an Amplified Laser Simplifies Heat Transfer Modeling To Determine the Thermal Transport Properties of Materials

Reid W. Wilson,[‡] Jack Kelleher-Ferguson,[‡] Eric C. Wu, and Benjamin J. Schwartz*

Cite This: https://doi.org/10.1021/acs.chemmater.6c01465

Read Online

ACCESS | Metrics & More | Article Recommendations | Supporting Information

ABSTRACT: Time-domain thermoreflectance (TDTR) is a pump−probe method typically used to measure both the cross-plane thermal conductivity (κ) of thin films and bulk materials and the thermal boundary conductance (σ) of material interfaces. Conventional TDTR relies on high-repetition-rate (MHz) ultrafast oscillators with low per-pulse energy, which require tightly focused pump beams to generate measurable thermoreflectance signals. This tight focusing necessitates thermal models with both lateral and cross-plane heat diffusion components that have strong sensitivity to the exact pump size. High repetition rates also cause heat buildup (pulse accumulation), requiring periodic steady-state thermal modeling, and, for thin films, modeling of heat flow into the substrate. This can be challenging for polymeric materials that exhibit anisotropic transport and often have very low κ and high surface roughness. Here, we introduce an approach built around a standard kHz rep-rate amplified ultrafast laser transient absorption setup, which we call femtosecond transient thermoreflectance (fs-TTR). The orders-of-magnitude higher per-pulse energy and lower repetition rate enable a simplified one-dimensional cross-plane heat transport model without pulse accumulation. The fs-TTR thermal model permits simultaneous fitting of κ and σ, which we demonstrate for materials spanning 4 orders of magnitude in thermal conductivity, including very low-κ polymer thin films. The direct measure of pump-on/pump-off changes in reflectivity, along with probing transient reflectance simultaneously at multiple wavelengths, makes fs-TTR an equal or, in some cases, an improved alternative to conventional oscillator-only TDTR.

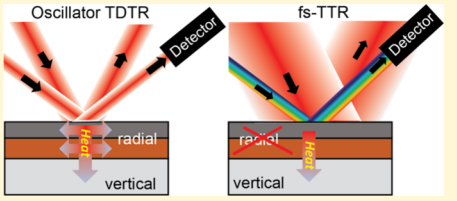

1. INTRODUCTION

Pump−probe thermoreflectance (TR) techniques, such as the time-domain (TDTR)[1,2] and frequency-domain (FDTR)[3] methods, are used in many fields to characterize the thermal properties of materials as well as the thermal behavior at interfaces. These noncontact, nondestructive methods for determining the thermal properties of thin films and their interfaces were first developed in the 1980s by research groups led by Eesley,[4−6] Rosencwaig,[7,8] and Maris.[9,10] Subsequent efforts led by Cahill[11−14] and Schmidt[15,16] in the 2000s resulted in significant improvements to TR techniques that have since become widely implemented to accurately thermally model a variety of material types, including within multilayer sample geometries.

Both TDTR and FDTR methods operate by utilizing a periodically modulated pump beam to deposit heat into a metal transducer and a probe beam to monitor the thermal response via the temperature-dependent reflectivity of the transducer. The TDTR method probes transient changes in surface reflectivity by controlling the time difference between pump and probe pulses,[1,2] whereas FDTR probes changes in the phase lag between periodic heating and the reflective thermal response of the transducer as a function of the modulation frequency of the pump.[3] The pump modulation frequency can be held constant in TDTR, but the specific frequency must be carefully selected to produce a thermal wave with the necessary penetration depth to probe the sample;[1,2] for example, probing nanometer-scale thin films requires megahertz pump modulation frequencies.

In transient TR methods, the change in probe reflectivity as a function of time monitors how heat leaves the transducer. At the earliest times, this depends on how heat diffuses within the transducer, but at longer time scales, the reflected probe signal is a function of how heat is transferred away from the transducer by the underlying material that is in thermal contact. The thermal models employed to fit thermoreflective decay data rely on either the thermal diffusivity, α, or the thermal effusivity, r, of the underlying material, as well as the thermal boundary conductance, σ, at the interface of the two materials. One can then use the value of α or r extracted from the TDTR measurement with a separately measured value of the volumetric heat capacity, C_v, to determine the thermal conductivity, κ, of the underlying material via[1]

Received: May 20, 2026
Revised: August 13, 2026
Accepted: August 18, 2026

$$\kappa = \alpha \cdot C_v = \frac{r^2}{C_v} \quad (1)$$

Sometimes, it is also possible to simultaneously fit values for C_v and κ if α (or r) is sufficiently uncorrelated to C_v.[16−19]

Although TR methods are capable of reliably determining the thermal properties of a vast array of materials, polymers and other low-thermal-conductivity (<1 W m^{-1} K^{-1}) materials are more difficult to thermally characterize due to inherently small changes in the thermoreflectance. Additionally, polymeric materials are often studied as thin (tens to hundreds of nanometers thick) films that are usually deposited onto substrates that have much higher thermal conductivities. This means that the study of polymeric materials often requires trilayer heat modeling to capture the heat diffusion through each of the transducer, polymer film, and substrate layers.[20] For conventional TDTR methods to be sensitive to σ, a sample must have a thickness similar to the Kapitza length, which is in the range of 1−10 nm for very low-κ polymers.[21,22] However, films this thin often have their TDTR signals dominated by the substrate response when the thermal penetration depth (determined by the modulation frequency) exceeds that of the film thickness.[1] Thus, the inability to probe both κ and σ in low thermal conductivity thin-film materials leads many researchers to choose a constant value for σ (rather than treat it as a parametrized variable) when determining κ is the measurement priority,[23−25] or to treat the thin film and both interfaces as a single in-series thermal resistor.[21,22]

Some limitations of the TDTR method stem from its use of ultrafast "oscillator"-type lasers, which have high repetition rates (a few MHz) and low per-pulse energies (~nJ). This means that the pump and probe pulses are focused to a small (typically a few tens of μm) spot size to generate signals that are measured with a lock-in amplifier. As a result, the modeling of the data needed to extract the thermal parameters of interest is complicated as it must account for both:[11,12,15] (1) the heat that is built up within the sample due to pulse accumulation, because the high repetition rate exceeds the kinetics of heat loss out of the sample and into the substrate; and (2) the radial and vertical diffusion of heat in the sample, because the small pump spot leads to both radial and vertical heat loss. Thus, TDTR experiments require precisely characterizing the pump beam radius, r_0, and also must differentiate the radial (κ_r, or a combination of in-plane κ_{xx} and κ_{yy}) and the vertical (cross-plane, κ_{zz}) thermal conductivity components when the probe is sensitive to radial heat diffusion. For conventional TDTR to assume 1-D (cross-plane) heat transport, both the modulation frequency and the pump/probe diameter ratio must be sufficiently high or large, respectively, depending on the thermal diffusivity of the underlying material.[26] Conversely, in the opposite limit, conventional TDTR may be utilized to resolve both radial and vertical thermal conductivity components with variable-spot-size or modulation-frequency-dependent studies.[26−28]

In this paper, we present a thermoreflectance method, femtosecond transient thermoreflectance (fs-TTR), that utilizes a chirped pulse-amplified[29−32] (hereafter referred to as just "amplified"), kHz repetition-rate, femtosecond pulse duration laser system instead of a MHz repetition-rate oscillator-type laser to simultaneously extract κ_{zz} and σ using a universal bilayer model for both bulk and thin-film materials beneath the transducer. Our method takes advantage of a simple retrofitting of standard ultrafast transient absorption (TA) setups that utilize amplified femtosecond lasers to probe reflectance instead of absorbance. Such TA setups usually can probe absorbance changes on the order of 10^{-4} ΔOD,[33−37] and here we use them to perform similarly sensitive thermoreflectance measurements that yield robust information about 1-D vertical heat diffusion.

As with standard TA setups,[33−37] our method directly probes pump-on, pump-off changes in reflectivity, $\Delta R = (R_{\text{pump on}} - R_{\text{pump off}})$, as a function of probe delay time using a mechanical delay stage. Although the low repetition rate is not conducive to lock-in amplification, the high pulse energies allow generation of a white-light continuum for the probe beam,[38,39] allowing the TR signal to be acquired at multiple wavelengths simultaneously to improve the signal-to-noise ratio. The lower repetition rate (typically a few kHz) and higher pulse energies (typically a few mJ) of amplified lasers allow for complete thermal equilibration between pulses and permit the use of a much larger pump spot size, which greatly simplifies the thermal modeling of the TDTR signals. The ability to isolate κ_{zz} relies on the fact that we can pump a much larger region than is probed, so that radial heat transport does not take place on the nanosecond time scales of the overall fs-TTR measurement.

Our fs-TTR method builds on but goes beyond the low repetition rate TDTR method presented by Larkin et al.,[40] which utilized a 250 kHz repetition-rate amplified laser system with a 4 μJ pulse energy, and detected the TR signal using lock-in amplification. Unlike the thermal model we present below, that used by Larkin et al. is sensitive only to the substrate and not to any thin-film samples of interest underneath the transducer in trilayer samples.[40] Our fs-TTR method is also distinct from previous ns- and ps-transient thermoreflectance experiments that utilize tens of kHz pulse repetition rates for exciting the samples of interest but employ a continuous-wave (CW) laser as the probe.[41−43] However, all of these previous TDTR and TTR methods, as well as our fs-TTR method, share similar advantages over oscillator-type TDTR, such as the elimination of heat buildup from pulse accumulation and more strict 1-D vertical heat diffusion sensitivity.[41,43]

In what follows, we show that performing transient thermoreflectance with an amplified transient absorption laser system (which is what we refer to as "fs-TTR") and using a correspondingly derived simplified thermal model allows accurate determination of both κ_{zz} for different materials that span 4 orders of magnitude in thermal conductivity (~0.10−100 W m^{-1} K^{-1}) and the σ of the transducer-underlying material interface, even for low-κ_{zz} polymer thin-film samples. Furthermore, we show that fs-TTR provides a multiwavelength detection advantage such that the signal can be integrated over a spectral range of wavelengths rather than the single wavelength available to oscillator-type TDTR. fs-TTR is capable of simultaneously determining values for both κ_{zz} and σ with equal or slightly higher certainty than measurements taken with oscillator-type TDTR. This is primarily due to simplifications of the thermal model afforded by using an amplified laser system, the minimization of noise-related uncertainty in fitted values of κ_{zz} and σ, and the dual-sensitivity of the model to locate solutions for both κ_{zz} and σ, which are anticorrelated in the 2-D parameter space.

https://doi.org/10.1021/acs.chemmater.6c01465
Chem. Mater. XXXX, XXX, XXX−XXX

2. THERMAL MODEL FOR fs-TTR UTILIZING AN AMPLIFIED ULTRAFAST TRANSIENT ABSORPTION SYSTEM

TDTR was originally developed utilizing oscillator-type laser systems that operate at pulse repetition rates of single to tens of MHz with pulses energies of ∼1 nJ, necessitating focused beam diameters on the order of tens or hundreds of micrometers.[6] The modeling of oscillator-driven TDTR data thus utilizes heat diffusion equations written in cylindrical coordinates to account for radial and vertical heat diffusion within the multilayer sample.[11,12,15] If the beam spot size, r_0, is well-characterized, the heat diffusion equations, including α and σ as fitting parameters, are solved using the thermal quadrupole approach:[1,44] the radial dependence of heat diffusion is converted to radial modes, with each radial mode becoming a separate vertical 1-D heat diffusion problem within the multilayered sample.

To our knowledge, TR measurements performed using an amplified ultrafast transient absorption system with a pump-on, pump-off detection method have not been presented in the literature. Thus, as mentioned above, our fs-TTR scheme differs from the low-rep-rate TDTR with an amplified laser demonstrated in ref 40; we also note that single-pulse TR measurements like fs-TTR are not the same as baseline-subtraction of the in-phase signal of conventional TDTR responses (see ref 45). In what follows, we present a thermal model for fs-TTR that incorporates the unique physics of amplified lasers with pulse energies in the mJ regime at a repetition rate of a few kHz. The high pulse energy allows the use of pump spot sizes on the order of many millimeters in diameter, while the low repetition rate prevents heat build-up in the sample between pulses. If the probe beam diameter remains small (less than hundreds of micrometers in comparison to the millimeter-sized pump), then the area around the probe is uniformly heated so that the temperature response of the probe is no longer sensitive to lateral heat diffusion. This means that only cross-plane heat diffusion modifies the temperature of the transducer in the probed area. The pump/probe beam size differences between oscillator-type TDTR and our fs-TTR method are qualitatively shown in Figure 1a and b.

TR methods rely on pumping an interband transition or plasmon resonance to deposit heat into the selected metal transducer. Modeling the heat delivered to the transducer by the pump is done by applying a variation of Beer−Lambert law, eq 2, adapted here from the work of Zhang et al.[46] To model temperature along a 1-D vertical grid, as depicted in Figure 2, the transducer is comprised of spatial depth points indexed at positions $i = 1$ to k, where $z_i = i \cdot \Delta z$, and at time-steps indexed by j, where $t_j = j \cdot \Delta t$ and $j = 0$ is the initial condition:

$$T_i^{j=0} = \frac{J(1 - R^{\text{pump}})}{C_v^{\text{met}} \delta^{\text{pump}}} \exp\left(-\frac{z_i}{\delta^{\text{pump}}}\right) \quad (2)$$

In eq 2, T is the absolute temperature at position z_i at time zero, J is the fluence of the pump beam, R^{pump} is the reflectance of the transducer at the pump wavelength, C_v^{met} is the volumetric heat capacity of the metal transducer, and δ^{pump} is the optical penetration depth of the pump wavelength. Throughout, we use the superscripts "met" and "sam" to denote that a particular variable is associated with the metal transducer or the underlying sample material of interest,

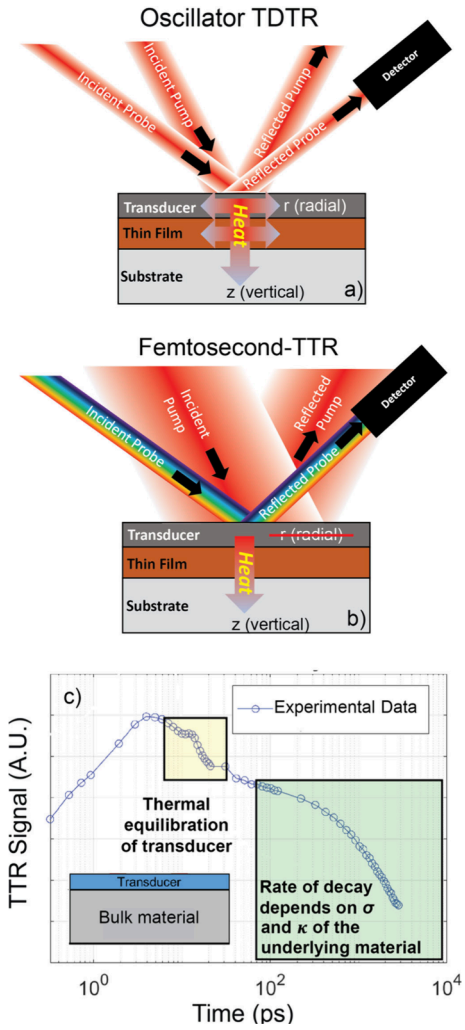

Figure 1. (a) Schematic of the common oscillator-based TDTR method. The small pump/probe spot size ratio results in the thermal response of the probe being sensitive not only to the laser spot size but also to heat diffusion in both the radial and vertical directions. (b) Schematic of the proposed amplified fs-TTR method presented in this work. The significantly larger pump/probe spot size ratio results in the thermal response of the probe being sensitive only to 1-D vertical heat diffusion. The rainbow coloring of the probe beam represents the ability of fs-TTR to have the thermoreflectance signal measured simultaneously at multiple wavelengths, as is typical in ultrafast transient absorption experiments, providing a signal-to-noise ratio advantage. (c) An example of fs-TTR data for an Al transducer on bulk silicon. The signal from 0 until ∼120 ps is dominated by thermalization of the transducer. After ∼120 ps, the signal depends only on the κ_{zz} and σ of the underlying material of interest, allowing the model described below to be fit to this portion of the data with a high degree of precision.

respectively. Equation 2 also assumes that no light interacts with the material beneath the transducer. Therefore, it is important that the transducer thickness is greater than roughly three optical penetration depths to ensure that ≥95% of the pump light is attenuated by the transducer.

Due to the sufficiently large pump−probe spot size ratio afforded by amplified systems, heat diffusion within the transducer and underlying material can be described using Fourier's equations for one-dimensional heat transport along the z-direction:

https://doi.org/10.1021/acs.chemmater.6c01465
Chem. Mater. XXXX, XXX, XXX−XXX

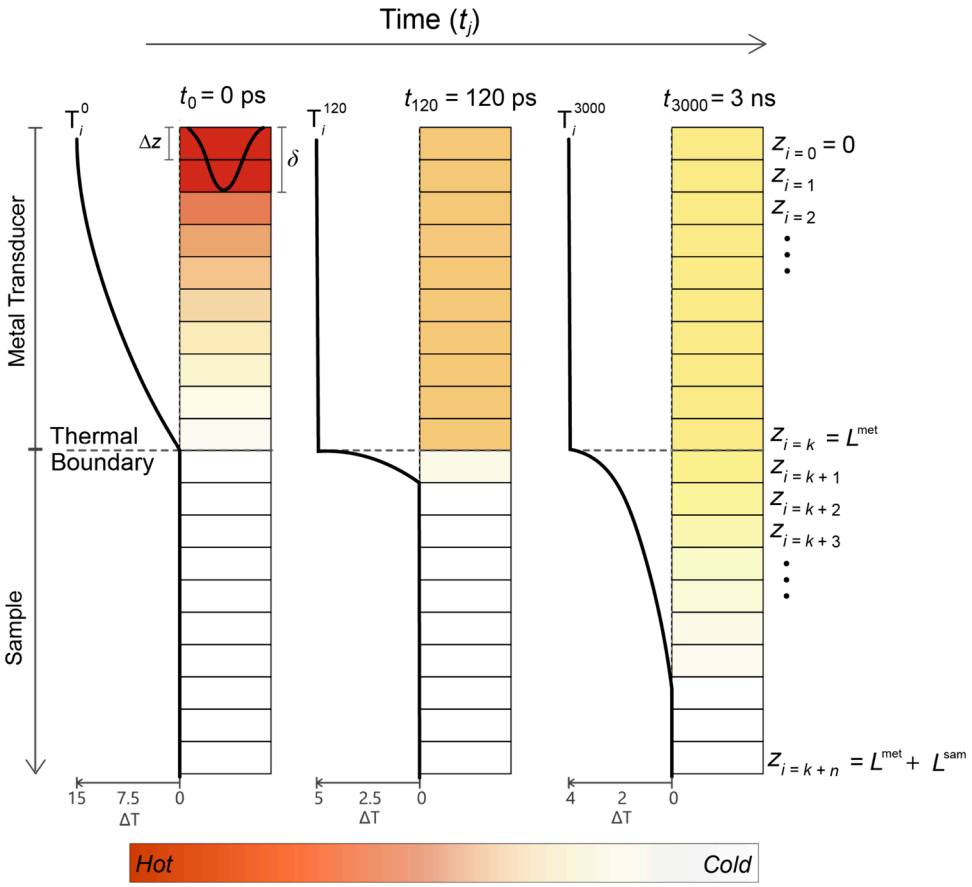

Figure 2. Discretized depiction of the 1-D thermal model for fs-TTR at different time stages. From left to right, t_0 = 0 ps corresponds to the point at which the transducer absorbs heat from the pump pulse, t_{120} corresponds to a time delay of 120 ps when the transducer has thermalized across its entire depth and heat is just beginning to enter the sample of interest, and t_{3000} corresponds to time delay of 3 ns where heat has diffused a significant distance into the underlying sample layer. The fitting parameters of the model include the thermal boundary conductance, σ, located at $z = L^{met}$, which quantifies the transfer of heat across the interface between the transducer and sample material, as well as α_{zz}^{sam}, which is the rate at which heat diffuses within the "zz" direction of the underlying sample material (cf. eq 1).

$$\frac{\partial T^{met}}{\partial t} = \alpha^{met}\frac{\partial^2 T^{met}}{\partial z^2} = \frac{\kappa^{met}}{C_v^{met}}\frac{\partial^2 T^{met}}{\partial z^2} \tag{3}$$

$$\frac{\partial T^{sam}}{\partial t} = \alpha_{zz}^{sam}\frac{\partial^2 T^{sam}}{\partial z^2} = \frac{\kappa_{zz}^{sam}}{C_v^{sam}}\frac{\partial^2 T^{sam}}{\partial z^2} \tag{4}$$

where t is the time after the pump pulse is incident on the transducer and T is the temperature. The cross-plane thermal diffusivity of the underlying sample material, α_{zz}^{sam}, is used as a fitting parameter to the fs-TTR data, which, in turn, yields the cross-plane thermal conductivity, κ_{zz}^{sam}, if the volumetric heat capacity of the sample material, C_v^{sam}, is known. We assume that the metal transducer is thermally isotropic and thus do not place a "zz" subscript on α^{met} and κ^{met}.

To solve eqs 3 and 4, we rewrite the equations so that space and time are discretized, as in eq 2, in a Crank–Nicolson finite differences formalism:[47]

$$-\alpha^{met}\frac{\Delta t}{\Delta z^2}T_{i-1}^{(j+1)} + 2\left(1 + \alpha^{met}\frac{\Delta t}{\Delta z^2}\right)T_i^{(j+1)} - \alpha^{met}\frac{\Delta t}{\Delta z^2}T_{i+1}^{(j+1)} = \alpha^{met}\frac{\Delta t}{\Delta z^2}T_{i-1}^{(j)} + 2\left(1 - \alpha^{met}\frac{\Delta t}{\Delta z^2}\right)T_i^{(j)} + \alpha^{met}\frac{\Delta t}{\Delta z^2}T_{i+1}^{(j)} \tag{5}$$

$$-\alpha_{zz}^{sam}\frac{\Delta t}{\Delta z^2}T_{i-1}^{(j+1)} + 2\left(1 + \alpha_{zz}^{sam}\frac{\Delta t}{\Delta z^2}\right)T_i^{(j+1)} - \alpha_{zz}^{sam}\frac{\Delta t}{\Delta z^2}T_{i+1}^{(j+1)} = \alpha_{zz}^{sam}\frac{\Delta t}{\Delta z^2}T_{i-1}^{(j)} + 2\left(1 - \alpha_{zz}^{sam}\frac{\Delta t}{\Delta z^2}\right)T_i^{(j)} + \alpha_{zz}^{sam}\frac{\Delta t}{\Delta z^2}T_{i+1}^{(j)} \tag{6}$$

where i indexes a particular z location with z = 0 at the top of the transducer, and j indexes a particular time after excitation, as shown in Figure 2. Heat transfer across the interface of the transducer-underlying material, located at thickness $z = L^{met}$, is then described by

$$-\kappa^{met}\left.\frac{\partial T^{met}}{\partial z}\right|_{z=L^{met}} = \sigma[T^{met}(L^{met}, t) - T^{sam}(L^{met}, t)] = -\kappa_{zz}^{sam}\left.\frac{\partial T^{sam}}{\partial z}\right|_{z=L^{met}} \tag{7}$$

where σ is the thermal boundary conductance, also typically used as a fitting parameter. In its discretized Crank–Nicolson form, eq 7 is written as

https://doi.org/10.1021/acs.chemmater.6c01465
Chem. Mater. XXXX, XXX, XXX−XXX

$$-\kappa^{\text{met}}\frac{-3T_k + 4T_{k-1} - T_{k-2}}{2\Delta z} = \sigma\left(\frac{4T_{k-1} - T_{k-2}}{3} - \frac{4T_{k+2} - T_{k+3}}{3}\right)$$

$$= -\kappa_{zz}^{\text{sam}}\frac{3T_{k+1} - 4T_{k+2} + T_{k+3}}{2\Delta z} \quad (8)$$

where the index k denotes the depth of the interface between the metal transducer and the underlying film, so that the spatial depth points representing the underlying sample run from $k + 1$ to $k + n$, as also depicted in Figure 2.

Due to the low repetition rate of amplified laser systems and the corresponding lack of pulse accumulation-induced heat build-up, we can safely assume in our model for most materials and thicknesses that 1) heat fully dissipates throughout the material layer(s) underneath the transducer in both bi- and trilayer sample geometries before the next pump pulse arrives, and 2) heat does not reach the back of the underlying film or substrate within the few-ns time window of the probe delay. This is specified mathematically by the adiabatic boundary condition:

$$\left.\frac{\partial T^{\text{sam}}}{\partial z}\right|_{z=L^{\text{sam}}} = 0 \quad (9)$$

where $z = L^{\text{sam}}$ is the distance coordinate of the backside of the underlying material layer. We show in Figure S8 in the SI that assumption (1) is easily tested by checking that the transient signal has fully recovered to baseline before the next pulse. We also discuss in Section S4 in the SI that assumption (2) can be verified by using our thermal model to predict the extent of heating through the underlying layer as a function of depth and time if rough values for κ_{zz}^{sam} are known (see Figure S13 in the SI).

The integrated probed temperature of the transducer, Θ, is then modeled using eq 10, which is rewritten as eq 11 in discretized form:

$$\Theta(t; \kappa_{zz}^{\text{sam}}, \sigma) = \int_0^{L^{\text{met}}} \exp\left(-\frac{z}{\delta^{\text{probe}}}\right)\cdot T^{\text{met}}(z, t)\, dz \quad (10)$$

$$\Theta(t_j; \kappa_{zz}^{\text{sam}}, \sigma) \approx \sum_{i=1}^{k} \exp\left(-\frac{z_i}{\delta^{\text{probe}}}\right)\cdot T_i^{(j)}\cdot\Delta z \quad (11)$$

This time-dependent spatially integrated transducer temperature is directly proportional to the fs-TTR signal, which is based on how the reflectance changes with the transducer temperature. The optical penetration depth of the probe light, δ^{probe}, determines how sensitive the probe is to the transducer temperature at a particular depth:

$$(R_{\text{pump on}}^{\text{probe}} - R_{\text{pump off}}^{\text{probe}}) = \Delta R^{\text{probe}}(t_j) \approx \left(\frac{dR^{\text{probe}}}{dT^{\text{met}}}\right)\Theta(t_j; \kappa_{zz}^{\text{sam}}, \sigma) \quad (12)$$

Thus, the change in reflectivity of the probe as a function of time, $\Delta R^{\text{probe}}(t_j)$, is proportional to $\Theta(t_j;\kappa_{zz}^{\text{sam}},\sigma)$ through the thermoreflectance coefficient of the metal transducer, $dR^{\text{probe}}/dT^{\text{met}}$.

To fit this thermal model to experimental fs-TTR data, we implement a nonlinear least-squares fitting algorithm (lsqnonlin in MATLAB) that optimizes the model fit via residual minimization:

$$\min \text{RSS}(\kappa_{zz}^{\text{sam}}, \sigma, c) = \sum_{j=1}^{N} [c\cdot y_j^{\text{data}} - \Theta(t_j; \kappa_{zz}^{\text{sam}}, \sigma)]^2 \quad (13)$$

where min RSS is the minimized square residual, N is the number of experimental time points, and y_j^{data} is the amplitude of an experimental thermoreflective signal at the jth time point. The fitting parameters are κ_{zz}^{sam} and σ, plus a scaling parameter c that normalizes the amplitude of the fs-TTR signal. The scaling factor avoids having to know precise numerical values for the laser fluence, J, and the thermoreflectance coefficient as model inputs, both of which would be necessary only to predict the magnitude of the signal. Because the fs-TTR signal amplitude scales linearly with pump power (see Figure S7 in the SI), we can use this simple scaling factor to match the signal amplitude generated by the model with experimentally acquired thermoreflective data.

To fit the thermal model to data, as is also necessary in conventional TDTR modeling, we must specify properties of the metal transducer, such as κ^{met}, C_v^{met}, the optical penetration depth, the percent reflectivity and the transducer thickness. For trilayer thin-film samples, the use of a universal bilayer model in performing fs-TTR necessitates that the thickness of the underlying material must be precisely measured to ensure that heat does not reach the substrate (or the second interface) within the few-ns time window of the probe delay. The MATLAB code that fits the model to data and solves for κ_{zz}^{sam} and σ is included in the SI/repository link.

We note that the fs-TTR model we present above is not designed to accurately account for short-time thermal phenomena such as acoustic echoes or hot electron carrier dynamics,[48,49] neither of which are required for studying the thermal behavior of the underlying material. Therefore, we fit our thermal model to thermoreflective data starting at a time delay of ~120 ps, after these more rapid processes are fully complete. Our model also does not need to account for radiative cooling, which can play a role in thermoreflectance measurements that take place on microsecond time scales,[41,43] because this type of heat transfer is negligible on the few ns-time scale of a fs-TTR experiment.

3. NOISE AND SENSITIVITY ANALYSIS OF THE fs-TTR THERMAL MODEL

In this section, we analyze how well the 1-D thermal model can extract κ_{zz}^{sam} and σ from fs-TTR data that has varying levels of noise. We do this by generating simulated signal data with preselected κ_{zz}^{sam} and σ values, adding selected amounts of Gaussian noise to the simulated signal, and then fitting the thermal model to this noisy data to test how well the model extracts the original values of κ_{zz}^{sam} and σ. We also perform a sensitivity analysis to understand correlations between the fit parameters, which we find differs from how these parameters behave in oscillator-type TDTR thermal models.

We investigated the model's sensitivity to noise across materials with a four-order-of-magnitude range of κ's, similar to what we measure experimentally with fs-TTR in Section 4

https://doi.org/10.1021/acs.chemmater.6c01465
Chem. Mater. XXXX, XXX, XXX−XXX

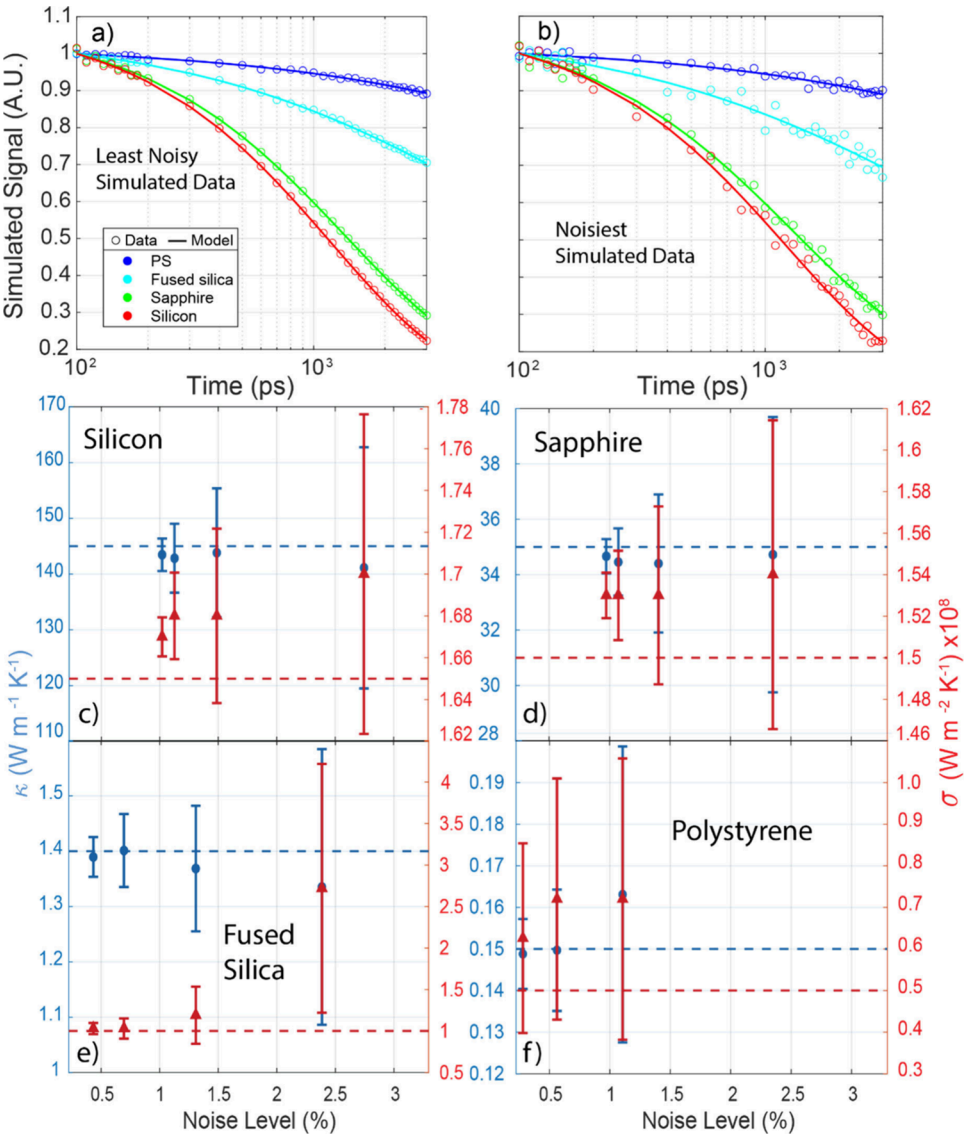

Figure 3. (a) Decay trace examples of simulated noisy data for four materials of interest at the lowest noise levels analyzed. b) Similar examples of simulated noisy data at the highest noise levels tested. c-f) κ_{zz}^{sam} and σ determined from fitting the fs-TTR thermal model for simulated noisy data emulating silicon (c), sapphire (d), fused silica (e) and polystyrene (f), each as a function of increasing percentage of added Gaussian noise. The noisy data was generated with a time interval of 10 ps between 120 and 200 ps and a time interval of 100 ps between 200 ps and 3 ns, respectively, as used in the experiments presented in Section 4. The red and blue dashed lines represent the initially simulated, "correct" values for κ_{zz}^{sam} and σ, respectively, whereas the error bars represent the standard deviation of the parameters extracted from 100 fitted datasets.

(below). For the sensitivity testing, we chose parameters to model the thermoreflectance signals of silicon, sapphire, fused silica, and polystyrene (see Table S2 of the SI), each with a 75-nm-thick Al transducer. After simulating the signals, we added Gaussian noise to the simulated data and then quantified the noise percentage (see Table S3 of the SI) as the average magnitude of root-mean-square (RMS) residuals relative to the noiseless simulated fs-TTR trace with the input values of κ_{zz}^{sam} and σ. In total, we generated 100 datasets for each simulated material at each of the multiple noise levels using datasets with the same time intervals and number of data points that we use experimentally below in Section 4. To test the reliability of the fs-TTR model as a function of noise level, we fit the model to the simulated noisy data and extracted κ_{zz}^{sam} and σ as the fitting parameters (see Figure S15 of the SI for a distribution of fitting results for a given sample at a single noise level).

Figure 3 displays examples of simulated data with the lowest and highest tested noise levels for each material (panels a,b) as well as the average κ_{zz}^{sam} and σ parameters extracted from 100 fitted datasets at each noise level for each material, with the raw standard deviation used as the error bars (panels c–f); see Section 5 in the SI for further details on how the noisy simulated data was generated and analyzed. For high-κ_{zz}^{sam}, high-σ samples (silicon and sapphire, Figures 3c and d), our results show that correct values (within 3% of the initially simulated input) for both κ_{zz}^{sam} and σ are obtained even through the 2%–3% noise regime. As the noise percentage level gets smaller, the variability (the standard deviation or error bars) in our extracted values also gets smaller and closer to the initially simulated "correct" values. This indicates that the model remains consistent even at elevated noise levels for high-κ_{zz}^{sam} materials, although we suggest using data with <1.5% noise to remain in the most accurate regime to fit κ_{zz}^{sam} and σ. We also

https://doi.org/10.1021/acs.chemmater.6c01465
Chem. Mater. XXXX, XXX, XXX−XXX

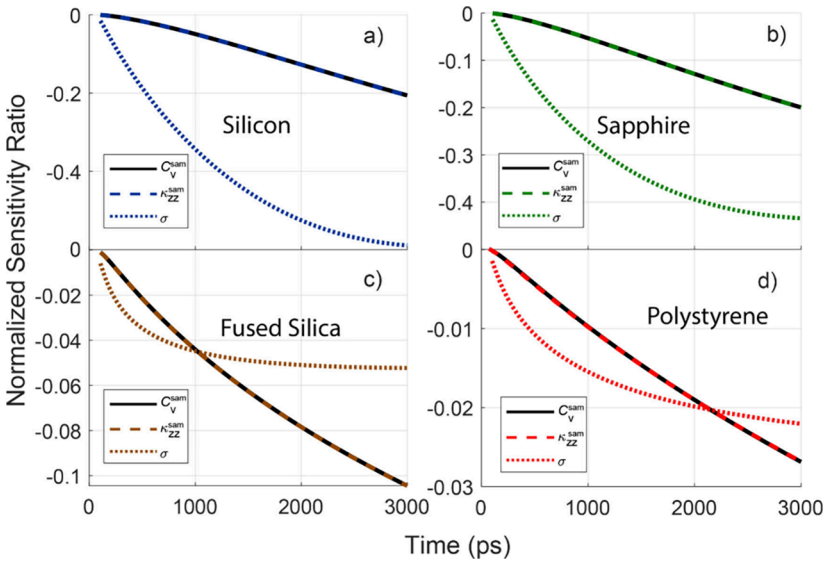

Figure 4. Sensitivity ratios, calculated using eq 14, for the thermal properties of C_v^{sam}, κ_{zz}^{sam}, and σ corresponding to the fs-TTR-simulated systems in Figure 3, including: (a) Al/silicon, (b) Al/sapphire, (c) Al/fused silica, and (d) Al/polystyrene. The sensitivity ratios for C_v^{sam} and κ_{zz}^{sam} are identical as fs-TTR measures the thermal diffusivity, which is composed of these two parameters (cf. eq 1). For lower-κ_{zz}^{sam} fused silica and polystyrene samples, the thermal boundary conductance, σ, has the most influence on the thermoreflectance signal at early delay times, while κ_{zz}^{sam} more strongly controls the fs-TTR decay at longer delay times. Conversely, for higher-κ_{zz}^{sam} silicon and sapphire samples, the thermal boundary conductance more strongly controls the thermoreflectance decay compared to κ_{zz}^{sam} across the entire selected probe delay range. See Figure S16 of the SI for additional sensitivity ratio curves for all other model input parameters.

observe an anticorrelation between the extracted values: if the average κ_{zz}^{sam} is slightly underestimated compared to the simulated value, then the average σ is slightly overestimated. This anticorrelation between the κ_{zz}^{sam} and σ parameters occurs with materials that have high thermal conductivities is particularly noticeable because both parameters affect the fs-TTR signal on similar time scales.

For simulated fused silica, which has a κ_{zz}^{sam} that is 2 orders of magnitude lower than silicon, the accuracy and reliability of the model fit is more impacted by noise. Above the 2% noise level, the model consistently yields values of σ that are higher than the initially simulated value, as seen in Figure 3e. Despite the overestimated average, however, the average fitted κ_{zz}^{sam} at the same noise level is <5% below the simulated value. This is because κ_{zz}^{sam} and σ become less correlated (more orthogonal) in lower-κ_{zz}^{sam} materials: as we show below, σ is more determined by the early time part of the transient signal in fs-TTR, while κ_{zz}^{sam} is more reflected in the longer-time part of the decay. We suggest only using data with <1% noise to remain in the most accurate regime to fit the κ_{zz}^{sam} and σ of low κ_{zz}^{sam} materials.

Finally, for simulated polystyrene, a polymeric material with an order of magnitude lower κ_{zz}^{sam} than fused silica, even relatively low (<1%) noise levels inhibit the ability of the model to accurately extract σ, as seen in Figure 3f. Like with fused silica, however, the fitted κ_{zz}^{sam} is less than 1% different from the simulated value below the 0.6% noise level and is less than 10% different at the ∼1% noise level. This observation reinforces the idea that with fs-TTR, κ_{zz}^{sam} and σ become increasingly decorrelated as the thermal conductivity of the sample material decreases. This means that fs-TTR can obtain accurate fitted values for κ_{zz}^{sam}, even if it is difficult to reliably extract σ due to high noise. If experimental data pertaining to very low-κ_{zz}^{sam} (<1 W m^{-1} K^{-1}) materials has too high of a noise level (above 0.5%) to reliably determine σ, one may choose to simply keep σ as a preselected input value that is held constant, as the choice of σ negligibly influences the fit of κ_{zz}^{sam}. This alternative approach, as mentioned above, is already the standard when performing oscillator-type TDTR measurements on very low-κ_{zz}^{sam} materials.[23−25]

Another way to show the dependence of the κ_{zz}^{sam} and σ fitting parameters in the 1-D fs-TTR model is by calculating sensitivity ratios. The sensitivity ratio (eq 14) quantitatively reveals the influence that a specific parameter has on the model fit with respect to the measured signal:

$$S_x(t_j) = \frac{\Theta_{x+\Delta x}(t_j) - \Theta_x(t_j)}{\frac{\Delta x}{x}\Theta_x(t_j)} = \frac{\Delta\Theta_x(t_j)}{\Theta_x(t_j)}\left(\frac{\Delta x}{x}\right)^{-1} \quad (14)$$

where $S_x(t_j)$ is the sensitivity ratio of model parameter x at the j^{th} time-step point and Δx is a small perturbation (usually single percentages). We normalized the sensitivity ratios, which are shown in Figure 4a−d, to allow better comparison of the relative sensitivity ratios for each parameter for the different simulated materials.

The sensitivity ratios we calculated using eq 14 show that, as an absolute value, $|S_\kappa^{sam}|$ increases as a function of fs-TTR delay time for all simulated materials. This is very different from oscillator-type TDTR, where $|S_\kappa^{sam}|$ peaks at early delay times and then decreases as a function of time.[1,50−53] Additionally, $S_\kappa^{sam}(t_j)$ is negative in fs-TTR but is typically positive in traditional oscillator-type TDTR.[1,52] This difference means that, in fs-TTR, a faster decay of the signal with time is directly correlated with higher κ_{zz}^{sam} values, so that longer delay times are more important for fitting accurate values of κ_{zz}^{sam} than shorter delay times. This also means that fs-TTR provides less sensitivity for lower-κ_{zz}^{sam} materials due to shallower signal decays, as is reflected in the S_κ^{sam} and S_σ for polystyrene, both of which are smaller in absolute value compared to materials with higher heat conduction. However, as demonstrated in Section 4 below, with sufficiently low-noise data, we are still able to

https://doi.org/10.1021/acs.chemmater.6c01465
Chem. Mater. XXXX, XXX, XXX−XXX

resolve both fitted values of κ_{zz}^{sam} and σ to reasonable certainties for very low-κ_{zz}^{sam} polymeric materials.

In the thermal model for fs-TTR, the sensitivities of the thermal conductivity and volumetric heat capacity, S_{κ}^{sam} and $S_{C_v}^{sam}$, are equal because the ratio of κ_{zz}^{sam} and σ is equal to α_{zz}^{sam}, as shown in eq 1. This fact means that fs-TTR requires C_v^{sam} to determine κ_{zz}^{sam}, as is also the case for high-modulation-frequency TDTR measurements.[1,2] For example, the modulated pump frequencies typically used in conventional TDTR cause S_{κ}^{sam} to match $S_{C_v}^{sam}$ as a function of probe delay time,[1] although the sensitivities of the two parameters begin to deviate below the 1−10 MHz regime.[1,18] Due to the nonzero $S_{C_v}^{sam}$ present in both fs-TTR and TDTR, any uncertainty in the measured value of C_v^{sam} will be propagated directly to the extracted fit values of κ_{zz}^{sam} and σ.

Since the real-value sensitivity ratios S_{κ}^{sam} and S_{σ} are both negative as a function of probe delay time in fs-TTR, an overestimation of one parameter results in the other parameter being underestimated, as shown by the spread of fitting results for κ_{zz}^{sam} and σ in Figure S15 in the SI, as well as above in Figure 3. However, in conventional TDTR, an overestimation of κ_{zz}^{sam} results in an overestimation in σ, as shown by Jiang et al.[1] This is because there is a difference in the behavior of the sensitivity ratios of the two methods: in conventional TDTR, S_{κ}^{sam} is a positive value that decreases toward 0 over time and S_{σ} is a decreasing value that turns from positive to negative as a function of time,[1] whereas these ratios are both negative and become more negative over time in fs-TTR.

We should note that both TDTR and fs-TTR share the requirement of having well-characterized transducer properties (L^{met}, C_v^{met} and κ^{met}) as model input parameters. This is because the thermoreflective signals measured by both methods are sensitive to the transducer properties, as shown by the fact that the transducer property sensitivity ratio values are on the same order or even larger than the sensitivity ratios for κ_{zz}^{sam} and σ. We provide a complete comparison of sensitivity ratios in Figure S16 of the SI for fs-TTR, while a similar analysis for oscillatory-type TDTR has been presented in work by both Jiang et al.[27] and Zhang et al.[54]

Overall, our sensitivity analysis shows that the ability to simultaneously extract both κ_{zz}^{sam} and σ is robust with the fs-TTR model. For fs-TTR, the fitting parameter σ has much greater influence on the overall signal (larger sensitivity) than κ_{zz}^{sam} at early times (≤1 ns), regardless of how well the system/underlying material transports heat. $|S_{\kappa}^{sam}|$ and $|S_{\sigma}|$ are larger in materials with higher κ_{zz}^{sam} and σ, whereas with lower thermal conductivity materials, S_{σ} has a smaller magnitude, reaching its plateau at earlier times. This results in $|S_{\kappa}^{sam}| > |S_{\sigma}|$ at longer delay times for our simulated fused silica and polystyrene systems. These differences, along with the fact that there are fewer fitting parameters and input values that can contribute to error, is what allows extracted values of κ_{zz}^{sam} and σ from fs-TTR to have similar or even lower uncertainty compared to conventional TDTR, as demonstrated in Section 4 below.

4. EXPERIMENTAL VALIDATION OF fs-TTR USING SAMPLES THAT SPAN FOUR ORDERS OF MAGNITUDE IN THERMAL CONDUCTIVITY

To verify that the model developed in Section 2 and an amplified laser can perform accurate thermal measurements, we fabricated five samples that span 4 orders of magnitude in thermal conductivity (~0.10 to hundreds of W m^{-1} K^{-1}). Simple bilayer (transducer/underlying material) samples of silicon (Si), sapphire (Al_2O_3), and fused silica (SiO_2) were fabricated by evaporating 100 ± 1 nm thick Al transducers directly on top of the material (see Section S1.2 in the SI for details). We also prepared thin-film, trilayer samples of polystyrene (PS) and poly(methyl methacrylate) (PMMA) by spin-casting these polymers onto silicon substrates followed by evaporation of a 100 ± 1 nm Al transducer (also see Section S1.2 in the SI for details).

The fs-TTR experiments we performed pumped the Al transducer at the 1.5 eV[87,88] peak of the interband transition and integrated the reflected white-light probe wavelengths over the range 900−915 nm; the results are shown as the circles in Figure 5. We determined that the probe wavelength range of 900−915 nm was optimal for our setup due to a convolution of the stability of the white-light continuum generated with our laser at different wavelengths and the high thermoreflective response of Al; we explore the use of this and other probe wavelength ranges in Section S3.1 in the SI (see Figures S10 and S11). In Figure 5, each sample was measured at one spot and the extracted values of the fitting parameters in Table 1 are from a single measurement. Our integrated signals averaged 30 000 or 60 000 shots per data point for samples with κ_{zz}^{sam} > 1 W m^{-1} K^{-1} or κ_{zz}^{sam} < 1 W m^{-1} K^{-1}, respectively, across the selected probe delay time window of 120 ps to 3 ns, with a time interval of 10 ps between 120−200 ps and a time interval of 100 ps between 200−3000 ps. This time window and data point interval selection is identical to the simulated data generated for the noise analysis of the thermal model discussed above in Section 3.

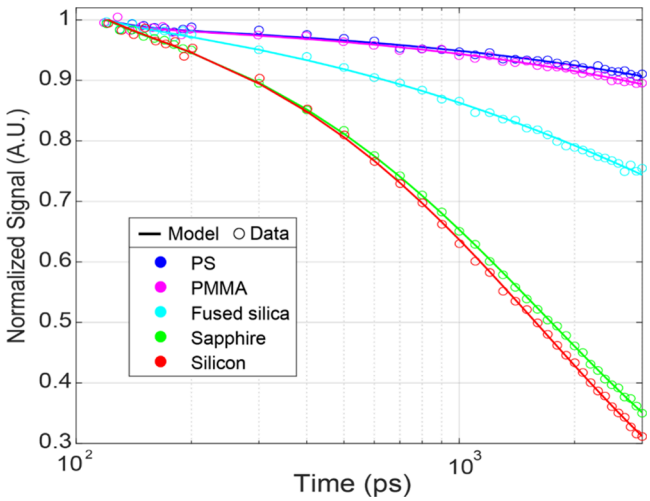

Figure 5. Experimental fs-TTR signal traces for silicon (red), sapphire (green), fused silica (aquamarine), PMMA (magenta), and PS (dark blue) samples, each with an evaporated 100-nm-thick Al transducer. The pump wavelength was 800 nm and the integrated probe wavelength range was 900−915 nm. The pump/probe spot area ratio was 70.5:1. The experimental data are the circles and the corresponding model fits are the solid curves. The percentage noise of each dataset, given in Table 1, was calculated using the RMS residuals of the data and the final model fit, the same way as in Figure 3. fs-TTR traces that include the early probe time-delay window (not included in model fits) are shown in Figure S9 in the SI. The minimized square residuals of the model fits are shown in Figure S12 in the SI.

https://doi.org/10.1021/acs.chemmater.6c01465
Chem. Mater. XXXX, XXX, XXX−XXX

Table 1. Fitted Values of κ_{zz}^{sam} and σ for Various Materials in Contact with Al Transducers Determined by Fitting the Data Taken with fs-TTR Shown in Figure 5 to the Model in Section 2, along with Literature Values for These Same Materials

	C_v^{sam} Input			Lit. κ_{zz}^{sam}			Lit. σ		
Material	value (J cm^{-3} K^{-1})	refs	Extracted κ_{zz}^{sam} (W m^{-1} K^{-1})[c]	value (W m^{-1} K^{-1})	refs	Extracted σ[c] (MW m^{-2} K^{-1})	value (MW m^{-2} K^{-1})	refs	Calculated % Noise[c]
Silicon (100)	1.66	18, 55	143 ± 10	130−152	18, 19, 56−58	161 ± 2	115−200	58−62	0.78%
Sapphire (0001; ∥ to c-axis)[a]	3.09	16, 63, 64	41.4 ± 1.4	38−42	65, 66	164 ± 2	134−350	10, 16, 67−69	0.46%
Fused Silica	1.65	18, 54, 70	1.31 ± 0.05	1.27−1.39	20, 54, 71, 72	136 ± 9	100−150	20	0.52%
PMMA	1.61	23, 24, 73−75	0.18(8) ± 0.02(2)	0.18−0.22	23, 24, 73−81	30 ± 4	No reports on Al/PMMA[b]		0.39%
PS	1.25	82, 83	0.15(3) ± 0.01(7)	0.14−0.16	24, 82−86	35 ± 7	∼20	82, 84, 85	0.41%

[a]The thermal conductivity anisotropy ratio range for sapphire in ref 65 was converted to values of κ_{zz}^{sam} by assigning 35 W m^{-1} K^{-1} to the direction perpendicular to the c-axis. [b]See section S6.4 in the SI for information on TBC measurements between PMMA and transducer metals other than Al. [c]This work; values were extracted from fitting the data in Figure 5 to the model in section 2.

The solid curves through the fs-TTR data points in Figure 5 are fits to the thermal model described in Section 2 (for all model input parameters, see Table S1 of the SI), and the extracted fit parameter values of κ_{zz}^{sam} and σ for each material, which are all consistent with values found in the literature, are given in Table 1. We calculated the uncertainty (±error) pertaining to fitted κ_{zz}^{sam} and σ values using the covariance of the Jacobian (which accounts for both noise in data as well as how many unknown variables are parametrized in the thermal model) from MATLAB's lsqnonlin fitting algorithm. For underlying materials with κ_{zz}^{sam} > 1 W m^{-1} K^{-1} and σ > 100 MW m^{-2} K^{-1}, our errors in κ_{zz}^{sam} and σ are 3%−7% and 1%−7%, respectively, which is an improvement over the 7%−12% error typically found in traditional oscillator-type TDTR methods.[50,89] In Table S4 and Figure S17 in Section S6.2 of the SI, we perform a detailed error propagation analysis for the fitted values of κ_{zz}^{sam} and σ based on uncertainty in the fs-TTR model input parameters. Additionally, we show in Table S5 in Section S6.3 of the SI that the fitted values of κ_{zz}^{sam} and σ for our samples are anticorrelated. Finally, we show in Figure S18 of the SI that large deviations in the fitted values of κ_{zz}^{sam} for the Al/Si and Al/sapphire samples only marginally changed the fitted values of σ, whereas for the Al/PMMA/Si and Al/PS/Si samples, multiplicative changes in σ cause κ_{zz}^{sam} to change by only a relatively tiny amount.

Our fs-TTR measurements on the very low-κ_{zz}^{sam} thin-film polymer samples, PS and PMMA, yielded errors in κ_{zz}^{sam} just above 10%, which is comparable to conventional TDTR,[50,89] and errors in σ as high as 20%. However, our ability to determine both parameters simultaneously at these uncertainty levels is also an improvement over conventional oscillator-type TDTR (where different modulation frequencies would be required to achieve different thermal penetration depths that are sensitive to the different parameters, effectively requiring κ_{zz}^{sam} and σ to be probed independently through separate measurements). We also note that with the signal averaging we implemented above, the noise percentage of our experimental data (calculated using the RMS residuals of the data and the final model fit) falls between 0.4%−0.8% for all five materials (see Table 1); these noise levels are low enough to provide very good fitting results based on the analysis in Section 3.

Silicon (cubic crystal structure) and fused silica (amorphous SiO_2 network) are thermally isotropic bulk materials,[66,90] which means that our measurements of κ_{zz}^{sam} are numerically equivalent to κ measurements that involve heat transfer through multiple axes of the material. On the other hand, single-crystal sapphire is thermally anisotropic ($\kappa_{xx} = \kappa_{yy} \neq \kappa_{zz}$),[65−67] which means that our measurement results depend on the orientation of the sapphire crystal. Here, we used a crystal cut along the 0001 plane, so that the transducer surface is perpendicular to the c-axis, meaning that our fs-TTR experiments report only on heat transfer along the c-axis. In the literature, κ measurements of bulk sapphire fall between 32−38 W m^{-1} K^{-1},[16,63,64,91−96] and the thermal conductivity anisotropy ratio between the c- and a-axes ranges from 1.08:1−1.18:1.[65] Our κ_{zz}^{sam} measurement along the c-axis of sapphire, 41.4 ± 1.4 W m^{-1} K^{-1}, is thus consistent with the literature, as it is higher than reported bulk values by 10%−20%, supporting the idea that our fs-TTR method is sensitive only to 1-D vertical heat transfer.

To validate the efficacy of our 1-D model and the use of fs-TTR on trilayer thin-film samples with low thermal conductivities, we examined two amorphous polymeric materials: PS and PMMA, shown as the blue and magenta curves in Figure 5, respectively. As spin-cast thin-films, PS and PMMA also display thermal anisotropy with in-plane thermal conductivities that are greater than those in the cross-plane direction.[81,86,97] Our extracted κ_{zz}^{sam} values for both materials fall well within error of values in the literature, as shown in Table 1. Our fitted value for the σ of Al/PS interface, in the 30s MW m^{-2} K^{-1}, is slightly higher than literature values (∼20 MW m^{-2} K^{-1}),[82,84,85] although variability in polymer surface roughness and/or metal deposition conditions can change the boundary conductance of metal−polymer interfaces by tens of MW m^{-2} K^{-1}.[21,22,98] To our knowledge, there is no reported thermal conductance measurement for Al/PMMA (see Section S6.4 in the SI for other studies performed on metal/PMMA interfaces). However, our inclusion of PMMA as a sample to compare to PS shows with fs-TTR, the κ_{zz}^{sam} of polymeric thin-films can be resolved down to hundredths of W m^{-1} K^{-1}. The ability of fs-TTR to extract values for σ with ≤20% uncertainty is a particularly notable result as our polymer films have thicknesses that are ∼10 times greater than their Kapitza lengths, so that σ would not be measurable in conventional oscillator-type TDTR. Overall, fs-TTR allows κ_{zz}^{sam} and σ values to be extracted with equal or lower uncertainty compared to conventional TDTR over at least four-orders-of-magnitude range in thermal conductivity.

https://doi.org/10.1021/acs.chemmater.6c01465
Chem. Mater. XXXX, XXX, XXX−XXX

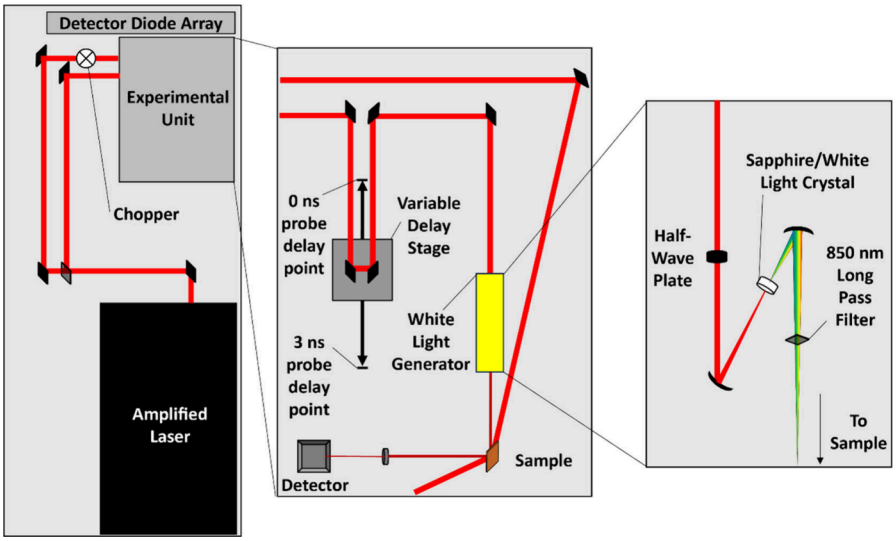

Figure 6. Schematic of a standard amplified ultrafast laser transient absorption system that was modified to perform measurements of fs-TTR signal in this work. The amplified laser beam is steered to a beam splitter to generate separate pump and probe beams. Both beams are steered into the experimental unit, although the pump beam goes through an optical chopper that only passes every other pulse. The only change to the setup from performing transient absorption is that the probe light is collected in reflection instead of transmission. Within the experimental unit, the probe beam is steered onto a variable delay stage to control the time delay. The probe beam is also steered through a half wave plate—its polarization relative to the pump beam is set to the magic angle (54.7°) and then focused into a sapphire plate to generate a white-light supercontinuum. This white-light probe is then focused tightly onto the sample where it is overlapped with the center of the chopped large-diameter pump beam. The transducer on the sample acts as a mirror to steer the probe beam through a focusing lens and into the multiwavelength detector. The signal is collected as the difference between pump-on and pump-off spectra on consecutive laser shots.

5. EXPERIMENTAL DETAILS FOR fs-TTR

One of the main advantages of fs-TTR is that it can use a standard amplified laser TA setup, where the only modification required is to collect the signal in reflection rather than transmission. We show a schematic of such a system in Figure 6, with specific details of our particular setup given in further detail in Section S1.3 in the SI. As with many TA systems, our amplified laser produces ∼3 mJ pulses of ∼40 fs duration at 800 nm at a 2 kHz repetition rate; the pulse energy and duration are sufficient to allow the use of nonlinear optics for generating other excitation wavelengths and for producing a white-light supercontinuum for probing multiple wavelengths simultaneously. The 800-nm output naturally generated by amplified Ti:sapphire systems is perfect for heating aluminum transducers as the interband transition for Al is located at 800 nm.[87,88] Additionally, the white-light probe in amplified systems can be tuned to spectrally overlap with aluminum's optimally high thermoreflectance region located in the near-infrared (850−1500 nm).[99,100] The time between the pump and probe pulses is controlled mechanically with a variable delay stage, allowing for time delays of up to 3 ns in our setup, which is still sufficient for TDTR even with low κ_{zz}^{sam} materials, as demonstrated in Section 4.

An important distinction between conventional TDTR and the fs-TTR method we present is the way that signal is detected. Conventional TDTR uses a lock-in amplifier to resolve both in-phase and out-of-phase signals at the chosen MHz modulation frequency; the ratio of the signals (V_{in}/V_{out}) yields a TDTR signal as a function of pump−probe delay.[1,2] Conversely, fs-TTR directly measures the reflected probe intensity for adjacent pump-on and pump-off shots and the signal directly measured is the change in reflectance, $\Delta R = (R_{pump\ on} - R_{pump\ off})$, as a function of pump−probe delay. The low repetition rate of the pump pulse (which is optically chopped at 1 kHz to be 50% of the probe repetition rate of 2 kHz) allows nearly every sample to return to ambient temperature equilibrium between the pump-on and pump-off probe pulses. The high energy of each pump pulse induces large enough changes in reflectivity, with single ΔmOD signals, that a lock-in amplifier is not necessary.

As mentioned above, the main advantage of having high amplified pulse energies is that the pump spot size can be large enough (many mm) to easily achieve 1-D vertical heat transport, as modeled above in Section 2 and demonstrated experimentally on both bulk (sapphire) and thin-film (PS and PMMA) thermally anisotropic materials in Section 4. To detect the point at lower pump/probe spot size ratios at which heat transport can no longer be treated with the 1-D model described in Section 2, we performed a series of TDTR measurements with different spot size ratios, as shown in Figure 7. Details of how we measured our pump and probe spot sizes are given in Sections S2.1 and S2.2 of the SI (see Figures S1−S5). For the measurements in Figure 7, we chose a very low-κ_{zz}^{sam} sample consisting of an Al transducer on thin-film PMMA on a Si substrate and found that the best-performing (largest signal) pump/probe spot area ratio was 70.5:1 (or 8.4:1 diameter ratio; red points in Figure 7). Since this ratio yielded an accurate value of κ_{zz}^{sam} for PMMA,[76] we performed fs-TTR using this ratio for each material studied in Section 4. We also found that the 1-D amplified fs-TTR model breaks down for the PMMA sample when the spot area ratio is ≤ 6.4:1 (or ≤ 2.5:1 diameter ratio). The blue points in Figure 7 show that at this 6.4:1 spot area ratio, the fs-TTR signal decays faster in time, producing an unphysically high fitted value for κ_{zz}^{sam}, compared to the measurement at the 70.5:1 spot area ratio. Failure of the 1-D thermal model at smaller spot area ratios is expected when the probe is large enough to sample the thermal gradient caused by the Gaussian spatial profile of the pump beam.

https://doi.org/10.1021/acs.chemmater.6c01465
Chem. Mater. XXXX, XXX, XXX−XXX

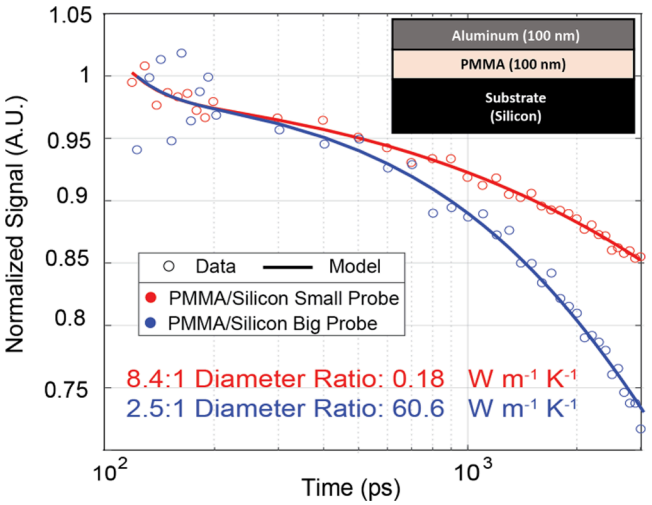

Figure 7. Experimental fs-TTR traces of an Al/PMMA/Si sample collected with different pump/probe diameter ratios; the red data are taken at the best-performing (for high signal intensity and signal-to-noise) diameter ratio of 8.4:1, whereas the blue data are taken using a pump/probe diameter ratio of 2.5:1, where the probe is large enough to experience nonflat portions of the Gaussian spatial profile of the pump beam. Our fs-TTR thermal model, which assumes 1-D vertical heat diffusion, can only fit correct values for κ_{zz}^{sam} if the pump/probe diameter ratio is >2.5:1. Note that the y-axis scale is highly expanded so that the absolute signal differences seen are relatively small. In both of these experiments, we pumped the Al transducer at 800 nm and probed the reflected response integrated between 900 and 915 nm. The pump diameter was fixed at 2952 μm and the diameter ratio was controlled by changing the size of the probe.

Of course, the spot area ratio at which the 1-D model breaks down will also depend on the thermal properties of the sample being studied, as samples with faster in-plane heat transport will need larger pump spot sizes. In Section S2.3 of the SI, we derive a model that allows one to predict pump−probe beam size ratios that are compatible with the 1-D thermal model from Section 2:

$$y = \frac{(r_{probe})^2}{[(r_{pump})^2 + (r_{probe})^2 + 8\alpha_{radial}t_{max}]} \quad (15)$$

In eq 15, y is the probe spatial averaging error fraction (i.e., the fraction of the temperature response being probed that is not experiencing the maximum pump intensity), r_{probe} and r_{pump} are the $1/e^2$ radii of the probe and pump beams, respectively, α_{radial} is the radial thermal diffusivity of the material/transducer being probed, and t_{max} is the maximum probe delay time. The larger the value of y, the worse the induced error from the heat distribution being nonuniform in the radial direction over the size of the probe.

As the probe beam is more tightly focused on the top of the Gaussian profile of the pump beam, and thus more strictly samples the peak power density of the pump, the value of y decreases to 0. Our 1-D thermal model breaks down if the probe: (1) becomes sensitive to lateral heat diffusion or (2) begins sampling thermal gradients due to the Gaussian spatial profile of the pump beam. If the pump spot radius is larger than hundreds of micrometers, then the lateral heat diffusion term, $8\alpha_{radial}\ t_{max}$, will be small compared to $(r_{pump})^2$ and thus will be negligible on the few-nanosecond time scale for materials with α_{radial} < 100 mm s^{-2}. Therefore, in the large pump diameter regime, the probe spatial averaging error fraction y is entirely dependent on the size of the probe beam. In Figure S6 of the SI, we show that the probe spatial averaging error fraction reaches the 10% threshold that we consider acceptable for fs-TTR measurements at a pump/probe diameter ratio of about 3:1. This is consistent with the ∼2.5:1 breakdown diameter ratio that we observed experimentally in Figure 7.

Another advantage of the low amplified laser repetition rate is that it allows the bilayer thermal model in Section 2 to be applied to thin-film (tens to hundreds of nanometers thick) samples without having to consider heat flow into the substrate. With the lack of pulse accumulation, a fs-TTR experiment can be tuned to prevent heat from a single pump pulse reaching the backside of the thin-film layer in a trilayer sample by either controlling the film thickness or selecting an appropriate probe delay time window. Ensuring that heat does not reach the backside of a thin-film sample within the probe delay window means that substrate effects will not influence the observed signal decay. In Section S4/Figures S13a and S13b of the SI, we show that, for very low-κ_{zz}^{sam} polymer samples, a minimum thickness of only 50 nm is necessary to prevent heat from reaching the substrate within the 3 ns probe delay of our system. Higher κ_{zz}^{sam} film samples will require larger thicknesses, but as long as this is achieved, our bilayer fs-TTR model does not require fitting the thermal boundary conductance of the thin-film/substrate interface.

6. CONCLUSIONS

In summary, we presented a method for thermoreflectance measurements that is designed around a standard amplified ultrafast laser transient absorption system, rather than the traditionally used oscillator-type system. fs-TTR provides the same time resolution as traditional oscillator-type TDTR, but the higher per-pulse pump energies and lower repetition rate provide significant benefits in the thermal modeling in terms of extracting the thermal conductivity and boundary conductance from the signals. The high pulse energies of amplified lasers allow for significantly greater pump/probe spot size ratios, which makes the heat transport under the probed region effectively one-dimensional, avoiding the need to incorporate both vertical and radial heat diffusion into the model. Furthermore, the use of a white-light probe allows the change in thermoreflectance to be integrated spectrally across a wavelength range, providing a signal-to-noise advantage that helps compensate for the lower repetition rate. The low repetition rate, however, provides the advantage that even thin-film samples with very low κ still have enough time to reach ambient equilibrium before the next pump pulse, so that there is no heat build-up due to pulse accumulation. This also reduces the number of interfaces and material layers that need to be thermally modeled in thin-film sample architectures.

To test the robustness of the simplified 1-D model for fitting fs-TTR data, we simulated Gaussian-noise-embedded data for a variety of materials with differing κ_{zz}^{sam} and σ across a range of noise levels. The model allows simultaneous fitting of κ_{zz}^{sam} and σ with an equal or lower uncertainty than conventional TDTR because in fs-TTR, each of these parameters relies on distinct probe time windows, as demonstrated by sensitivity analysis. We also verified that the assumptions of the 1-D model are easily met experimentally, and that we can readily measure values of κ_{zz}^{sam} and σ for materials with values spanning over 4 orders of magnitude. Overall, we believe that fs-TTR, an

https://doi.org/10.1021/acs.chemmater.6c01465
Chem. Mater. XXXX, XXX, XXX−XXX

experimental setup that can be constructed trivially from a lab that is already setup to do ultrafast transient absorption spectroscopy, provides a great alternative with potential advantages over the oscillator-type version of this experiment.

■ ASSOCIATED CONTENT

Data Availability Statement

The raw data and the code used for data and error analysis are publicly available at the following repository: htpps://doi.org/10.5061/dryad.hdr7sqw07.

Supporting Information

The Supporting Information is available free of charge at https://pubs.acs.org/doi/10.1021/acs.chemmater.6c01465.

Additional experimental details, materials, methods and simulations (PDF)

■ AUTHOR INFORMATION

Corresponding Author

Benjamin J. Schwartz − *Department of Chemistry and Biochemistry, University of California, California 90095-1569, United States;* orcid.org/0000-0003-3257-9152; Email: bjs@g.ucla.edu

Authors

Reid W. Wilson − *Department of Chemistry and Biochemistry, University of California, California 90095-1569, United States*

Jack Kelleher-Ferguson − *Department of Chemistry and Biochemistry, University of California, California 90095-1569, United States*

Eric C. Wu − *Department of Chemistry and Biochemistry, University of California, California 90095-1569, United States*

Complete contact information is available at: https://pubs.acs.org/10.1021/acs.chemmater.6c01465

Author Contributions

‡Authors R. W. Wilson and J. Kelleher-Ferguson contributed equally to this work. All authors have given approval to the final version of the manuscript.

Funding

This work was supported by NSF Grant Nos. DMR-2513790 and CHE-2247583.

Notes

The authors declare no competing financial interest.

■ REFERENCES

(1) Jiang, P.; Qian, X.; Yang, R. Tutorial: Time-Domain Thermoreflectance (TDTR) for Thermal Property Characterization of Bulk and Thin Film Materials. *J. Appl. Phys.* **2018**, *124* (16), 161103.

(2) Mohan, R.; Khan, S.; Wilson, R. B.; Hopkins, P. E. Time-Domain Thermoreflectance. *Nat. Rev. Methods Primer* **2025**, *5* (1), 55.

(3) Kirsch, D. J.; Martin, J.; Warzoha, R.; McLean, M.; Windover, D.; Takeuchi, I. An Instrumentation Guide to Measuring Thermal Conductivity Using Frequency Domain Thermoreflectance (FDTR). *Rev. Sci. Instrum.* **2024**, *95* (10), 103006.

(4) Eesley, G. L. Observation of Nonequilibrium Electron Heating in Copper. *Phys. Rev. Lett.* **1983**, *51* (23), 2140−2143.

(5) Eesley, G. L. Generation of Nonequilibrium Electron and Lattice Temperatures in Copper by Picosecond Laser Pulses. *Phys. Rev. B* **1986**, *33* (4), 2144−2151.

(6) Paddock, C. A.; Eesley, G. L. Transient Thermoreflectance from Thin Metal Films. *J. Appl. Phys.* **1986**, *60* (1), 285−290.

(7) Opsal, J.; Rosencwaig, A.; Willenborg, D. L. Thermal-Wave Detection and Thin-Film Thickness Measurements with Laser Beam Deflection. *Appl. Opt.* **1983**, *22* (20), 3169−3176.

(8) Opsal, J.; Rosencwaig, A. Thermal and Plasma Wave Depth Profiling in Silicon. *Appl. Phys. Lett.* **1985**, *47* (5), 498−500.

(9) Thomsen, C.; Strait, J.; Vardeny, Z.; Maris, H. J.; Tauc, J.; Hauser, J. J. Coherent Phonon Generation and Detection by Picosecond Light Pulses. *Phys. Rev. Lett.* **1984**, *53* (10), 989−992.

(10) Stoner, R. J.; Maris, H. J. Kapitza Conductance and Heat Flow between Solids at Temperatures from 50 to 300 K. *Phys. Rev. B* **1993**, *48* (22), 16373−16387.

(11) Cahill, D. G.; Goodson, K.; Majumdar, A. Thermometry and Thermal Transport in Micro/Nanoscale Solid-State Devices and Structures. *J. Heat Transfer* **2002**, *124* (2), 223−241.

(12) Cahill, D. G. Analysis of Heat Flow in Layered Structures for Time-Domain Thermoreflectance. *Rev. Sci. Instrum.* **2004**, *75* (12), 5119−5122.

(13) Costescu, R. M.; Wall, M. A.; Cahill, D. G. Thermal Conductance of Epitaxial Interfaces. *Phys. Rev. B* **2003**, *67* (5), 054302.

(14) Huxtable, S.; Cahill, D. G.; Fauconnier, V.; White, J. O.; Zhao, J.-C. Thermal Conductivity Imaging at Micrometre-Scale Resolution for Combinatorial Studies of Materials. *Nat. Mater.* **2004**, *3* (5), 298−301.

(15) Schmidt, A. J.; Chen, X.; Chen, G. Pulse Accumulation, Radial Heat Conduction, and Anisotropic Thermal Conductivity in Pump-Probe Transient Thermoreflectance. *Rev. Sci. Instrum.* **2008**, *79* (11), 114902.

(16) Schmidt, A. J.; Cheaito, R.; Chiesa, M. A Frequency-Domain Thermoreflectance Method for the Characterization of Thermal Properties. *Rev. Sci. Instrum.* **2009**, *80* (9), 094901.

(17) Abdallah, Z.; Pomeroy, J. W.; Blasakis, N.; Baltopoulos, A.; Kuball, M. Simultaneous Measurement of Thermal Conductivity and Volumetric Heat Capacity of Thermal Interface Materials Using Thermoreflectance. *ACS Appl. Electron. Mater.* **2024**, *6* (7), 5183−5189.

(18) Liu, J.; Zhu, J.; Tian, M.; Gu, X.; Schmidt, A.; Yang, R. Simultaneous Measurement of Thermal Conductivity and Heat Capacity of Bulk and Thin Film Materials Using Frequency-Dependent Transient Thermoreflectance Method. *Rev. Sci. Instrum.* **2013**, *84* (3), 034902.

(19) Chen, T.; Song, S.; Shen, Y.; Zhang, K.; Jiang, P. Simultaneous Measurement of Thermal Conductivity and Heat Capacity across Diverse Materials Using the Square-Pulsed Source (SPS) Technique. *Int. Commun. Heat Mass Transfer* **2024**, *158*, 107849.

(20) Zhu, J.; Tang, D.; Wang, W.; Liu, J.; Holub, K. W.; Yang, R. Ultrafast Thermoreflectance Techniques for Measuring Thermal Conductivity and Interface Thermal Conductance of Thin Films. *J. Appl. Phys.* **2010**, *108* (9), 094315.

(21) Losego, M. D.; Moh, L.; Arpin, K. A.; Cahill, D. G.; Braun, P. V. Interfacial Thermal Conductance in Spun-Cast Polymer Films and Polymer Brushes. *Appl. Phys. Lett.* **2010**, *97* (1), 011908.

(22) Sandell, S.; Maire, J.; Chávez-Ángel, E.; Sotomayor Torres, C. M.; Kristiansen, H.; Zhang, Z.; He, J. Enhancement of Thermal Boundary Conductance of Metal-Polymer System. *Nanomaterials* **2020**, *10* (4), 670.

(23) Xie, X.; Li, D.; Tsai, T.-H.; Liu, J.; Braun, P. V.; Cahill, D. G. Thermal Conductivity, Heat Capacity, and Elastic Constants of Water-Soluble Polymers and Polymer Blends. *Macromolecules* **2016**, *49* (3), 972−978.

(24) Xie, X.; Yang, K.; Li, D.; Tsai, T.-H.; Shin, J.; Braun, P. V.; Cahill, D. G. High and Low Thermal Conductivity of Amorphous Macromolecules. *Phys. Rev. B* **2017**, *95* (3), 035406.

(25) Walwil, H. M.; Zhao, Y.; Koh, Y. K. Accurate Thermal Conductivity Measurements of Porous Thin Films by Time-Domain Thermoreflectance. *ACS Appl. Mater. Interfaces* **2024**, *16* (2), 2861−2867.
(26) Hopkins, P. E.; Serrano, J. R.; Phinney, L. M.; Kearney, S. P.; Grasser, T. W.; Harris, C. T. Criteria for Cross-Plane Dominated Thermal Transport in Multilayer Thin Film Systems During Modulated Laser Heating. *J. Heat Transfer* **2010**, *132* (8), 081302.
(27) Jiang, P.; Qian, X.; Yang, R. Time-Domain Thermoreflectance (TDTR) Measurements of Anisotropic Thermal Conductivity Using a Variable Spot Size Approach. *Rev. Sci. Instrum.* **2017**, *88* (7), 074901.
(28) Jiang, P.; Qian, X.; Gu, X.; Yang, R. Probing Anisotropic Thermal Conductivity of Transition Metal Dichalcogenides MX2 (M = Mo, W and X = S, Se) Using Time-Domain Thermoreflectance. *Adv. Mater.* **2017**, *29* (36), 1701068.
(29) Mourou, G. Nobel Lecture: Extreme Light Physics and Application. *Rev. Mod. Phys.* **2019**, *91* (3), 030501.
(30) Strickland, D.; Mourou, G. Compression of Amplified Chirped Optical Pulses. *Opt. Commun.* **1985**, *56* (3), 219−221.
(31) Maine, P.; Mourou, G. Amplification of 1-Nsec Pulses in Nd:Glass Followed by Compression to 1 Psec. *Opt. Lett.* **1988**, *13* (6), 467−469.
(32) Maine, P.; Strickland, D.; Bado, P.; Pessot, M.; Mourou, G. Generation of Ultrahigh Peak Power Pulses by Chirped Pulse Amplification. *IEEE J. Quantum Electron.* **1988**, *24* (2), 398−403.
(33) Johnston, C. R.; Puskar, N. G.; Vargas-Hurlston, I. Z.; Eichmann, K. G.; Wang, Q.; Modak, A.; Javed, J. M.; Arcidiacono, A.; King, S. B. Ultrabroadband Transient Absorption Spectroscopy with Sub-25 μOD Sensitivity and Double Differential Scatter and Noise Rejection. *Opt. Express* **2026**, *34* (12), 22393−22403.
(34) He, S.; Jin, P.; Lian, T.; Zhu, H. Transient Absorption Spectroscopy. *Nat. Rev. Methods Primer* **2026**, *6* (1), 34.
(35) Hussain, M.; Batool, S.; Mahmood, Z.; Rehmat, N.; El-Zohry, A. M.; Zhao, J.; Di Donato, M.; Hartman, M. C. T.; Tibbetts, K. M. Transient Absorption Spectroscopy: A Mechanistic Tool for Triplet Sensitizers and Their Applications. *Chem. Soc. Rev.* **2026**, *55* (4), 1862−1890.
(36) Tamai, Y.; Murata, Y.; Natsuda, S.; Sakamoto, Y. How to Interpret Transient Absorption Data?: An Overview of Case Studies for Application to Organic Solar Cells. *Adv. Energy Mater.* **2024**, *14* (7), 2301890.
(37) Wu, E. C.; Vidales, D. G.; Salamat, C. Z.; Duong, Q. M.; León Ruiz, A.; Ready, A. D.; Mehmedović, Z.; Stanfield, D. A.; Spokoyny, A. M.; Tolbert, S. H.; Schwartz, B. J. Ultrafast Transient Absorption Studies of the Dynamics of Free and Coulombically Trapped Polarons in Doped Conjugated Polymers. *Adv. Funct. Mater.* **2025**, *35* (51), No. e07480.
(38) Brodeur, A.; Chin, S. L. Ultrafast White-Light Continuum Generation and Self-Focusing in Transparent Condensed Media. *JOSA B* **1999**, *16* (4), 637−650.
(39) Imran, T.; Figueira, G. Intensity-Phase Characterization of White-Light Continuum Generated in Sapphire by 280 Fs Laser Pulses at 1053 Nm. *J. Opt.* **2012**, *14* (3), 035201.
(40) Larkin, L. S.; Smoyer, J. L.; Norris, P. M. Laser Repetition Rate in Time-Domain Thermoreflectance Techniques. *Int. J. Heat Mass Transfer* **2017**, *109*, 786−790.
(41) Garrelts, R.; Marconnet, A.; Xu, X. Assessment of Thermal Properties via Nanosecond Thermoreflectance Method. *Nanoscale Microscale Thermophys. Eng.* **2015**, *19* (4), 245−257.
(42) Yuan, C.; Waller, W. M.; Kuball, M. Nanosecond Transient Thermoreflectance Method for Characterizing Anisotropic Thermal Conductivity. *Rev. Sci. Instrum.* **2019**, *90* (11), 114903.
(43) Jeong, J.; Meng, X.; Rockwell, A. K.; Bank, S. R.; Hsieh, W.-P.; Lin, J.-F.; Wang, Y. Picosecond Transient Thermoreflectance for Thermal Conductivity Characterization. *Nanoscale Microscale Thermophys. Eng.* **2019**, *23* (3), 211−221.
(44) Maillet, D.; Andre, S.; Batsale, J.-C.; Degiovanni, A. *Thermal Quadrupoles: Solving the Heat Equation through Integral Transforms*; Wiley, 2000.
(45) Jiang, P.; Qian, X.; Yang, R. A New Elliptical-Beam Method Based on Time-Domain Thermoreflectance (TDTR) to Measure the in-Plane Anisotropic Thermal Conductivity and Its Comparison with the Beam-Offset Method. *Rev. Sci. Instrum.* **2018**, *89* (9), 094902.
(46) Zhang, C.; Bi, K.; Wang, J.; Ni, Z.; Chen, Y. Measurement of Thermal Boundary Conductance between Metal and Dielectric Materials Using Femtosecond Laser Transient Thermoreflectance Technique. *Sci. China Technol. Sci.* **2012**, *55* (4), 1044−1049.
(47) Crank, J.; Nicolson, P. A Practical Method for Numerical Evaluation of Solutions of Partial Differential Equations of the Heat-Conduction Type. *Math. Proc. Camb. Philos. Soc.* **1947**, *43* (1), 50−67.
(48) Hopkins, P. E.; Duda, J. C.; Kaehr, B.; Wang Zhou, X.; Peter Yang, C.-Y.; Jones, R. E. Ultrafast and Steady-State Laser Heating Effects on Electron Relaxation and Phonon Coupling Mechanisms in Thin Gold Films. *Appl. Phys. Lett.* **2013**, *103* (21), 211910.
(49) Wilson, R. B.; Coh, S. Parametric Dependence of Hot Electron Relaxation Timescales on Electron-Electron and Electron-Phonon Interaction Strengths. *Commun. Phys.* **2020**, *3* (1), 179.
(50) Yang, J.; Ziade, E.; Schmidt, A. J. Uncertainty Analysis of Thermoreflectance Measurements. *Rev. Sci. Instrum.* **2016**, *87* (1), 014901.
(51) Wei, C.; Zheng, X.; Cahill, D. G.; Zhao, J.-C. Invited Article: Micron Resolution Spatially Resolved Measurement of Heat Capacity Using Dual-Frequency Time-Domain Thermoreflectance. *Rev. Sci. Instrum.* **2013**, *84* (7), 071301.
(52) Chen, T.; Jiang, P. Decoupling Thermal Properties in Multilayered Systems for Advanced Thermoreflectance Experiments. *Phys. Rev. Appl.* **2025**, *23* (4), 044004.
(53) Jiang, P.; Huang, B.; Koh, Y. K. Accurate Measurements of Cross-Plane Thermal Conductivity of Thin Films by Dual-Frequency Time-Domain Thermoreflectance (TDTR). *Rev. Sci. Instrum.* **2016**, *87* (7), 075101.
(54) Zhang, M.; Chen, T.; Song, S.; Bao, Y.; Guo, R.; Zheng, W.; Jiang, P.; Yang, R. Extending the Low-Frequency Limit of Time-Domain Thermoreflectance via Periodic Waveform Analysis. *J. Appl. Phys.* **2025**, *138* (5), 055101.
(55) Flubacher, P.; Leadbetter, A. J.; Morrison, J. A. The Heat Capacity of Pure Silicon and Germanium and Properties of Their Vibrational Frequency Spectra. *Philos. Mag. J. Theor. Exp. Appl. Phys.* **1959**, *4* (39), 273−294.
(56) Inyushkin, A. V.; Taldenkov, A. N.; Gibin, A. M.; Gusev, A. V.; Pohl, H.-J. On the Isotope Effect in Thermal Conductivity of Silicon. *Phys. Status Solidi C* **2004**, *1* (11), 2995−2998.
(57) Ho, C. Y.; Powell, R. W.; Liley, P. E. Thermal Conductivity of the Elements. *J. Phys. Chem. Ref. Data* **1972**, *1* (2), 279−421.
(58) Cheaito, R.; Gaskins, J. T.; Caplan, M. E.; Donovan, B. F.; Foley, B. M.; Giri, A.; Duda, J. C.; Szwejkowski, C. J.; Constantin, C.; Brown-Shaklee, H. J.; Ihlefeld, J. F.; Hopkins, P. E. Thermal Boundary Conductance Accumulation and Interfacial Phonon Transmission: Measurements and Theory. *Phys. Rev. B* **2015**, *91* (3), 035432.
(59) Gorham, C. S.; Hattar, K.; Cheaito, R.; Duda, J. C.; Gaskins, J. T.; Beechem, T. E.; Ihlefeld, J. F.; Biedermann, L. B.; Piekos, E. S.; Medlin, D. L.; Hopkins, P. E. Ion Irradiation of the Native Oxide/Silicon Surface Increases the Thermal Boundary Conductance across Aluminum/Silicon Interfaces. *Phys. Rev. B* **2014**, *90* (2), 024301.
(60) Hopkins, P. E.; Phinney, L. M.; Serrano, J. R.; Beechem, T. E. Effects of Surface Roughness and Oxide Layer on the Thermal Boundary Conductance at Aluminum/Silicon Interfaces. *Phys. Rev. B* **2010**, *82* (8), 085307.
(61) Hopkins, P. E.; Beechem, T.; Duda, J. C.; Hattar, K.; Ihlefeld, J. F.; Rodriguez, M. A.; Piekos, E. S. Influence of Anisotropy on Thermal Boundary Conductance at Solid Interfaces. *Phys. Rev. B* **2011**, *84* (12), 125408.
(62) Stevens, R. J.; Smith, A. N.; Norris, P. M. Measurement of Thermal Boundary Conductance of a Series of Metal-Dielectric

Interfaces by the Transient Thermoreflectance Technique. *J. Heat Transfer* **2005**, *127* (3), 315−322.
(63) Burghartz, St.; Schulz, B. Thermophysical Properties of Sapphire, AlN and MgAl2O4 down to 70 K. *J. Nucl. Mater.* **1994**, *212*−*215*, 1065−1068.
(64) Dobrovinskaya, E. R.; Lytvynov, L. A.; Pishchik, V. Properties of Sapphire. In *Sapphire: Material, Manufacturing, Applications*; Pishchik, V., Lytvynov, L. A., Dobrovinskaya, E. R., Eds.; Springer US: Boston, MA, 2009; pp 55−176, DOI: 10.1007/978-0-387-85695-7_2.
(65) Slack, G. A. Thermal Conductivity of MgO, Al_2O_3, $MgAl_2O_4$, and Fe_3O_4 Crystals from 3° to 300°K. *Phys. Rev.* **1962**, *126* (2), 427−441.
(66) Wang, D.; Ban, H.; Jiang, P. Three-Dimensional (3D) Tensor-Based Methodology for Characterizing 3D Anisotropic Thermal Conductivity Tensor. *Int. J. Heat Mass Transfer* **2025**, *242*, 126886.
(67) Rahman, M.; Shahzadeh, M.; Braeuninger-Weimer, P.; Hofmann, S.; Hellwig, O.; Pisana, S. Measuring the Thermal Properties of Anisotropic Materials Using Beam-Offset Frequency Domain Thermoreflectance. *J. Appl. Phys.* **2018**, *123* (24), 245110.
(68) Hopkins, P. E.; Salaway, R. N.; Stevens, R. J.; Norris, P. M. Temperature-Dependent Thermal Boundary Conductance at Al/Al2O3 and Pt/Al2O3 Interfaces. *Int. J. Thermophys.* **2007**, *28* (3), 947−957.
(69) Blank, M.; Weber, L. Towards a Coherent Database of Thermal Boundary Conductance at Metal/Dielectric Interfaces. *J. Appl. Phys.* **2019**, *125* (9), 095302.
(70) Brückner, R. Properties and Structure of Vitreous Silica. I. *J. Non-Cryst. Solids* **1970**, *5* (2), 123−175.
(71) Combis, P.; Cormont, P.; Gallais, L.; Hebert, D.; Robin, L.; Rullier, J.-L. Evaluation of the Fused Silica Thermal Conductivity by Comparing Infrared Thermometry Measurements with Two-Dimensional Simulations. *Appl. Phys. Lett.* **2012**, *101* (21), 211908.
(72) Wray, K. L.; Connolly, T. J. Thermal Conductivity of Clear Fused Silica at High Temperatures. *J. Appl. Phys.* **1959**, *30* (11), 1702−1705.
(73) Assael, M. J.; Botsios, S.; Gialou, K.; Metaxa, I. N. Thermal Conductivity of Polymethyl Methacrylate (PMMA) and Borosilicate Crown Glass BK7. *Int. J. Thermophys.* **2005**, *26* (5), 1595−1605.
(74) Rudtsch, S.; Hammerschmidt, U. Intercomparison of Measurements of the Thermophysical Properties of Polymethyl Methacrylate. *Int. J. Thermophys.* **2004**, *25* (5), 1475−1482.
(75) Wang, X.; Liman, C. D.; Treat, N. D.; Chabinyc, M. L.; Cahill, D. G. Ultralow Thermal Conductivity of Fullerene Derivatives. *Phys. Rev. B* **2013**, *88* (7), 075310.
(76) Kim, I.; Burzo, M. G.; Komarov, P. L.; Raad, P. E. Thermal Conductivity Measurements of Ultra-Thin Amorphous Poly(Methyl Methacrylate) (PMMA) Films. In *ASME 2013 International Mechanical Engineering Congress and Exposition*; Heat Transfer and Thermal Engineering, Vol. *8C*; ASME: San Diego, CA, USA, 2014, DOI: 10.1115/IMECE2013-66507.
(77) Assael, M. J.; Antoniadis, K. D.; Wu, J. New Measurements of the Thermal Conductivity of PMMA, BK7, and Pyrex 7740 up to 450K. *Int. J. Thermophys.* **2008**, *29* (4), 1257−1266.
(78) Tye, R. P.; Salmon, D. R. Thermal Conductivity Certified Reference Materials Pyrex 7740 and Polymethylmethacrylate. In *Proceedings of the 26th Thermal Conductivity Conference - and 14th Thermal Expansion Joint Conferences*; DEStech Publications, Inc.: Cambridge, 2001; pp 437−451.
(79) Boumaza, T.; Redgrove, J. Use of the Transient Plane Source Technique for Rapid Multiple Thermal Property Measurements. *Int. J. Thermophys.* **2003**, *24* (2), 501−512.
(80) Putnam, S. A.; Cahill, D. G.; Ash, B. J.; Schadler, L. S. High-Precision Thermal Conductivity Measurements as a Probe of Polymer/Nanoparticle Interfaces. *J. Appl. Phys.* **2003**, *94* (10), 6785−6788.
(81) Yamaguchi, S.; Shiga, T.; Ishioka, S.; Saito, T.; Kodama, T.; Shiomi, J. Anisotropic Thermal Conductivity Measurement of Organic Thin Film with Bidirectional 3ω Method. *Rev. Sci. Instrum.* **2021**, *92* (3), DOI: 10.1063/5.0030982.
(82) Liu, J.; Ju, S.; Ding, Y.; Yang, R. Size Effect on the Thermal Conductivity of Ultrathin Polystyrene Films. *Appl. Phys. Lett.* **2014**, *104* (15), 153110.
(83) Kiessling, A.; Simavilla, D. N.; Vogiatzis, G. G.; Venerus, D. C. Thermal Conductivity of Amorphous Polymers and Its Dependence on Molecular Weight. *Polymer* **2021**, *228*, 123881.
(84) Zheng, K.; Sun, F.; Tian, X.; Zhu, J.; Ma, Y.; Tang, D.; Wang, F. Tuning the Interfacial Thermal Conductance between Polystyrene and Sapphire by Controlling the Interfacial Adhesion. *ACS Appl. Mater. Interfaces* **2015**, *7* (42), 23644−23649.
(85) Zheng, K.; Sun, F.; Zhu, J.; Ma, Y.; Li, X.; Tang, D.; Wang, F.; Wang, X. Enhancing the Thermal Conductance of Polymer and Sapphire Interface via Self-Assembled Monolayer. *ACS Nano* **2016**, *10* (8), 7792−7798.
(86) Katz, J. S.; Barako, M. T.; Park, W.; Sood, A.; Asheghi, M.; Goodson, K. E. Highly Anisotropic Thermal Conductivity in Spin-Cast Polystyrene Nano-Films. In *17th IEEE Intersociety Conference on Thermal and Thermomechanical Phenomena in Electronic Systems (ITherm)*; 2018; pp 477−481, DOI: 10.1109/ITHERM.2018.8419509.
(87) Smith, D. Y.; Segall, B. Intraband and Interband Processes in the Infrared Spectrum of Metallic Aluminum. *Phys. Rev. B* **1986**, *34* (8), 5191−5198.
(88) Bennett, H. E.; Bennett, J. M.; Ashley, E. J. Infrared Reflectance of Evaporated Aluminum Films. *JOSA* **1962**, *52* (11), 1245−1250.
(89) Koh, Y. K.; Singer, S. L.; Kim, W.; Zide, J. M. O.; Lu, H.; Cahill, D. G.; Majumdar, A.; Gossard, A. C. Comparison of the 3ω Method and Time-Domain Thermoreflectance for Measurements of the Cross-Plane Thermal Conductivity of Epitaxial Semiconductors. *J. Appl. Phys.* **2009**, *105* (5), 054303.
(90) McCarter, D. R.; Paquin, R. A. Isotropic Behavior of an Anisotropic Material: Single Crystal Silicon. In *Material Technologies and Applications to Optics, Structures, Components, and Sub-Systems*, Vol. *8837*; SPIE, 2013; pp 44−53. DOI: 10.1117/12.2025770.
(91) Cahill, D. G.; Lee, S.-M.; Selinder, T. I. Thermal Conductivity of κ-Al2O3 and α-Al2O3 Wear-Resistant Coatings. *J. Appl. Phys.* **1998**, *83* (11), 5783−5786.
(92) Monchamp, R. R. Preparation and Properties of Crystalline Laser Oxide Materials. *J. Solid State Chem.* **1975**, *12* (3), 201−206.
(93) Cheng, Z.; Koh, Y. R.; Ahmad, H.; Hu, R.; Shi, J.; Liao, M. E.; Wang, Y.; Bai, T.; Li, R.; Lee, E.; Clinton, E. A.; Matthews, C. M.; Engel, Z.; Yates, L.; Luo, T.; Goorsky, M. S.; Doolittle, W. A.; Tian, Z.; Hopkins, P. E.; Graham, S. Thermal Conductance across Harmonic-Matched Epitaxial Al-Sapphire Heterointerfaces. *Commun. Phys.* **2020**, *3* (1), 115.
(94) Hoque, M. S. B.; Koh, Y. R.; Aryana, K.; Hoglund, E. R.; Braun, J. L.; Olson, D. H.; Gaskins, J. T.; Ahmad, H.; Elahi, M. M. M.; Hite, J. K.; Leseman, Z. C.; Doolittle, W. A.; Hopkins, P. E. Thermal Conductivity Measurements of Sub-Surface Buried Substrates by Steady-State Thermoreflectance. *Rev. Sci. Instrum.* **2021**, *92* (6), 064906.
(95) Cahill, D. G.; Pohl, R. O. Lattice Vibrations and Heat Transport in Crystals and Glasses. *Annu. Rev. Phys. Chem.* **1988**, *39*, 93−121.
(96) Minnich, A.; Chen, G. Quasi-Ballistic Heat Transfer From Metal Nanostructures on Sapphire; American Society of Mechanical Engineers Digital Collection, 2011, DOI: 10.1115/AJTEC2011-44094.
(97) Katz, J. S.; Park, W.; Barako, M. T.; Sood, A.; Asheghi, M.; Goodson, K. E. Nanostencil Fabrication with Double Exposure Optical Lithography for Scalable Resist-Free Patterning of Metal on Polymers. In *2018 Solid-State, Actuators, and Microsystems Workshop Technical Digest*; Transducer Research Foundation: Hilton Head, SC, USA, 2018; pp 280−283, DOI: 10.31438/trf.hh2018.80.
(98) Wang, S.; Ren, L.; Han, M.; Zhou, W.; Wong, C.; Bai, X.; Sun, R.; Zeng, X. Molecular Design of a Highly Matched and Bonded

Interface Achieves Enhanced Thermal Boundary Conductance. *Nanoscale* **2023**, *15* (19), 8706−8715.
(99) Ujihara, K. Reflectivity of Metals at High Temperatures. *J. Appl. Phys.* **1972**, *43* (5), 2376−2383.
(100) Wilson, R. B.; Apgar, B. A.; Martin, L. W.; Cahill, D. G. Thermoreflectance of Metal Transducers for Optical Pump-Probe Studies of Thermal Properties. *Opt. Express* **2012**, *20* (27), 28829−28838.

https://doi.org/10.1021/acs.chemmater.6c01465
Chem. Mater. XXXX, XXX, XXX−XXX